Critical evolution of a finite system

M. Belkacem, V. Latora, and A. Bonasera
INFN–Laboratorio Nazionale del Sud, Viale Andrea Doria (ang. Via S. Sofia), 95123 Catania, Italy
(Received 30 September 1994)

In this work, we investigate the possibility of occurrence of a critical behavior related to a liquid-gas phase transition in a finite classical system. The equation of state of such a classical system resembles that of nuclear matter. Through a study of mass distributions, scaled factorial moments, anomalous fractal dimensions, and moments of cluster mass distributions, we find evidence for the presence of a critical behavior of our finite system. Such a critical behavior is connected, by the use of Fisher's droplet model and Campi analysis, to a liquid-gas phase transition.

PACS number(s): 25.70.−z, 05.70.Fh, 25.75.+r, 64.70.Fx

I. INTRODUCTION

The possibility of occurrence of a critical behavior related to a liquid-gas phase transition in the fragmentation of hot nuclear systems has been the subject of several investigations that study the transition from the liquid like phase of ordinary nuclear matter (as encountered at low excitation energies) to a gaseous phase [1–4]. Theoretical studies indicate that infinite nuclear matter has an equation of state very similar to that of a van der Waals gas which is characterized by the existence of a liquid-gas phase transition [5–8]. Recent experiments in heavy-ion reactions at energies around the Fermi energy have revealed the creation of many fragments in the final stages of the reaction exhibiting a power law in fragment mass distributions [9]. Such a power law, as described by the droplet model of Fisher [10], is expected for droplet condensation near the critical temperature, indicating a liquid to gas phase transition. Of course one would like to know if the detected fragments have something to do with the predicted phase transition. Strictly speaking, sharp phase transitions can only occur in the thermodynamic limit in that the critical singularities appear only for a system with a very large number of particles. In particular in small systems like two colliding nuclei (where only a few hundreds of nucleons are involved) the fluctuations can completely wash out the phase transition. Especially important in this context is the role of the long-range Coulomb field. We note that the Coulomb field restricts the natural mass of the biggest nucleus to about 250 nucleons. Therefore we expect that the behavior of a finite system is changed if this system is charged as well.

Assuming that a critical behavior is possible, the problem is how to find evidence for it from the large amount of experimental data. In this paper, we address both problems and demonstrate that finite systems may in fact exhibit a critical behavior that can be revealed through a study of inclusive mass distributions, scaled factorial moments, anomalous fractal dimensions, and through the analysis of conditional moments as developed by Campi [11,12].

An exact solution of the quantum many-body problem is presently out of sight and this is especially true for the nuclear systems. The dynamical approaches available give the time evolution of the one-body distribution function as in TDHF or the semiclassical analog, i.e., the Vlasov equation [13]. This is clearly not sufficient when the system enters the spinodal region and long-range correlations become important to form blobs of matter [14]. On the other hand the exact classical many-body problem can be quite easily solved for a system made of about 100–400 particles. In classical molecular dynamics all correlations are present; therefore, we can gain important information from a detailed dynamical study. The important problem is to try to understand what the role of quantum fluctuations would be. Naively one would expect that quantum effects smooth any sharp transition that can be present in the classical limit. However, if excitation energies are large and densities are small then the classical limit may be a good approximation.

This paper is organized as follows. In Sec. II, we give a brief description of the classical model used in this study. We study in Sec. III the mass distributions by the use of the droplet model of Fisher. Section IV is devoted to the intermittency analysis together with the study of anomalous fractal dimensions. Section V contains the study of moments of fragment mass distributions in terms of Campi analysis. Section VI deals with the role of the Coulomb force in the time evolution of the system. Finally in Sec. VII, we study the time evolution of the different observables and of the critical behavior and give our summary and conclusions in Sec. VIII.

II. CLASSICAL MOLECULAR DYNAMICS

In this model we assume that the nucleus is made up of A nucleons that behave classically. These particles move under the influence of a two-body potential V given by [15]

$$V_{np}(r) = V_r[\exp(-\mu_r r)/r - \exp(-\mu_r r_c)/r_c] - V_a[\exp(-\mu_a r)/r - \exp(-\mu_a r_a)/r_a] ,$$
$$V_{nn}(r) = V_{pp}(r) = V_0[\exp(-\mu_0 r)/r - \exp(-\mu_0 r_c)/r_c] . \quad (1)$$

r_c=5.4 fm is a cutoff radius. V_{np} is the potential acting between a neutron and a proton while V_{nn} is the potential acting between two identical nucleons. The first potential is attractive at large r and repulsive at small r, while the latter is purely repulsive so no bound state of identical nucleons can exist. This is done in order to mimic somehow the Pauli principle. The values of the parameters entering the Yukawa potentials are given in Ref. [15] and give a corresponding equation of state (EOS) of classical matter having about 250 MeV of compressibility (set M in Ref. [15]). This EOS strikingly resembles that of nuclear matter [i.e., equilibrium density $\rho_0 = 0.16$ fm^{-3} and energy $E(\rho_0) = -16$ MeV/nucleon]. Furthermore, in Refs. [15,16], it is shown that many experimental data on heavy-ion collisions are reasonably explained by this classical model. Of course this is not accidental but it is due to the accurate choice of the parameters of the two-body potentials.

The classical Hamilton's equations of motion are solved using the Taylor method at the order $O[(\delta t)^3]$ where δt is the integration time step [17]. Energy and momentum are well conserved. The nucleus is initialized in its ground state by using the frictional cooling method [18]. Afterward, it is excited at a temperature T giving a Maxwellian velocity distribution to its nucleons by means of a Metropolis sampling [17]. We have studied the disassembly of two different systems, (A=100, Z=50) and (A=400, Z=200) starting from an initial density ρ=0.125 fm^{-3} and with different values of the initial temperature. In our calculations, the Coulomb interaction is not taken into account, apart in Sec. VI.

In Fig. 1 we plot the time evolution of the two systems in the density temperature (ρ, T) plane. In the plot the full lines give the isothermal (ITS—isothermal spinodal) and isentropic (AS—adiabatic spinodal) spinodal regions of our classical system. They are given by

$$\left.\frac{\partial^2 E(\rho)}{\partial \rho^2}\right|_T = 0 \,, \qquad \left.\frac{\partial^2 E(\rho)}{\partial \rho^2}\right|_S = 0 \,. \tag{2}$$

The point at T=15 MeV and ρ=0.05 fm^{-3} in both graphs gives the critical point for the liquid gas phase transition in an infinite system. Note again the strong resemblance to the (predicted) EOS of nuclear matter. The dashed lines give the values for isentropic expansion.

In the calculations density and temperature are determined following Ref. [19]. Since in the initial stage the system is not perfectly equilibrated, the expansion turns out to be not isentropic. But quickly (after about 5 fm/c) the system equilibrates and the following expansion is isentropic. We discuss first the T=2 MeV case. This is a typical case of evaporation: the system expands and emits particles. Quickly the expansion comes to a halt and the system oscillates back and forth while it cools down through particles emission. It is important to note that the system enters the region of instability of infinite matter. Finite size effects reduce such a region and shift it to lower densities. Already the ground state of our system has a density lower than the equilibrium value for the infinite system.

At higher temperatures the system enters deeply into the instability region. In particular for the highest temperatures, 15 and 20 MeV, the densities reached are sometimes outside the instability region from the gas side. This implies that there is a quick expansion which leads the system in the gas region and then small drops start to form. This is approximately true for all the expansions at T larger than 5–6 MeV. For lower temperatures the system never hits the gas region and bubbles form from the liquid side.

In the upper part of Fig. 2 we plot the time evolution of the number of fragments (dashed line) and number of IMF's (dashed-dotted line) per unit time averaged over 100 events for the expansion of the system A=100 starting with an initial density ρ=0.125 fm^{-3} and temperature T=5 MeV. In the medium part of the figure we plot the total multiplicity (dashed line), and intermediate mass fragment (IMF) multiplicity (dashed-dotted line), together with the mass of the biggest fragment (solid line) versus time. The lower part of Fig. 2 shows the standard deviation of these quantities around the averages. One sees clearly three phases in this time evolution. At the beginning, the different quantities remain constant until the system enters the region of dynamical instabilities (around 20–30 fm/c). In the second phase, the dynamical phase, from 30 to 200 fm/c, the three observables change

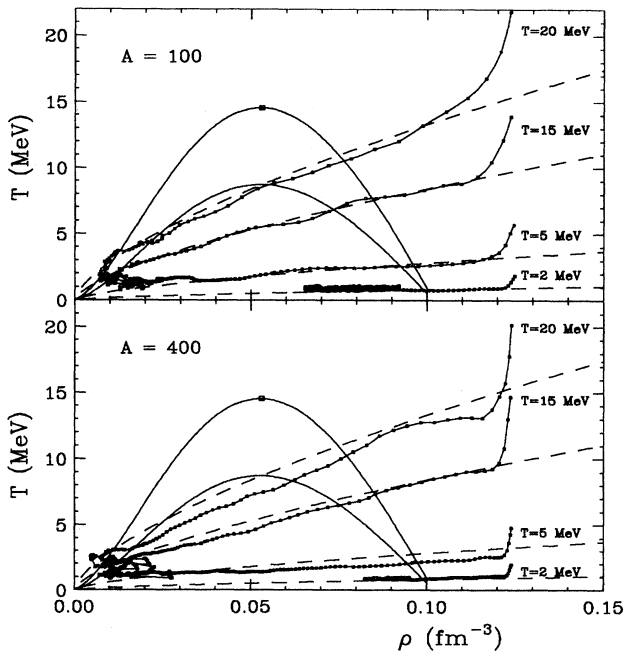

FIG. 1. Expansion of a system with A=100 (upper part) and A=400 (lower part) particles starting from temperatures T=2, 5, 15, and 20 MeV. The average temperature of the biggest fragment is plotted versus its average density. Full dots are at a time interval of 1 fm/c. Solid curves are the ITS (top) and the AS (bottom) lines and dashed curves give the values for an isentropic expansion.

rapidly. The mass of the biggest fragment goes down from 100 to 30–35. The total multiplicity increases from 1 to 20 and the IMF multiplicity from 1 to 4. In this phase, the fluctuations of the total and IMF multiplicities reach their maximum while the fluctuations of the mass of the biggest fragment show a bump around 100–150 fm/c. In the last phase, the evaporation-deexcitation phase, the IMF multiplicity remains constant while the mass of the biggest fragment decreases slowly. The fragments formed in the dynamical phase cool down by emitting particles,

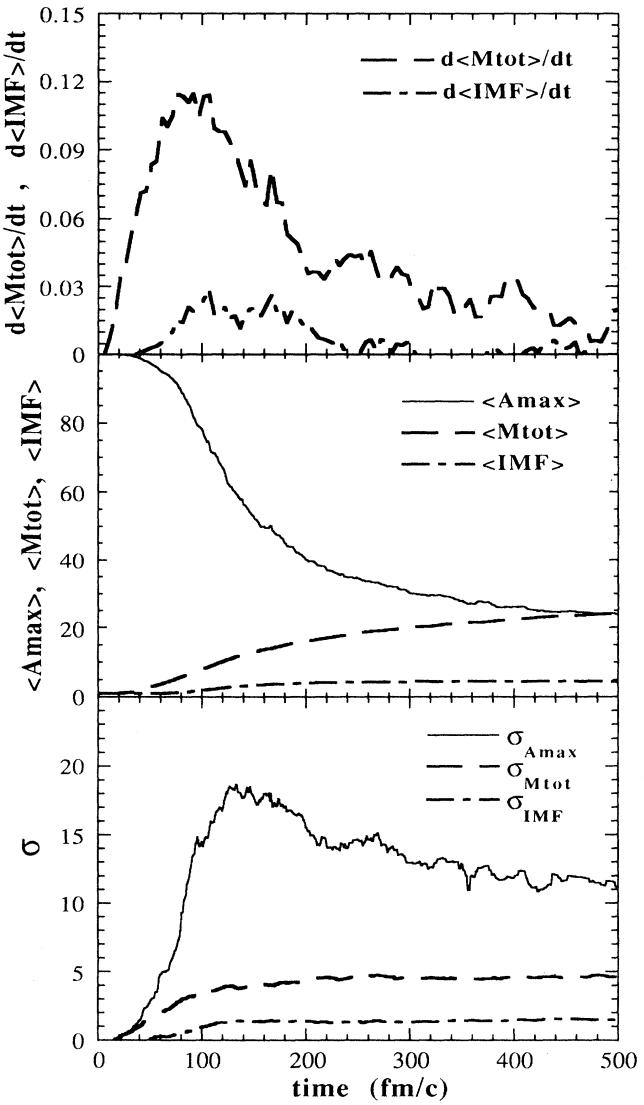

FIG. 2. Time evolution of the mass of the biggest fragment, total multiplicity, and IMF multiplicity averaged over 100 events for the expansion of the system A=100 starting with ρ=0.125 fm^{-3} and T=5 MeV. The upper part shows the time evolution of the number of fragments (dashed line) and the number of IMF's (dashed-dotted line) [in (fm/c)$^{-1}$]. The medium part shows the time integrated values of the total multiplicity (dashed line) and IMF multiplicity (dashed-dotted line), together with the mass of the biggest fragment. In the lower part we plot the standard deviation around the averages of the three quantities.

which explains the slow increase of the total multiplicity in this phase.

III. FISHER'S DROPLET MODEL AND MASS DISTRIBUTIONS

The droplet model of Fisher is a model of liquid-gas phase transition in which one tries to determine when a liquid-gas system favors the growth of large liquid droplets, and when it favors the dissociation of those droplets into a vapor [10]. In this model, the probability of formation of droplets can be estimated by calculating the change in the Gibbs free energy of the system when a droplet appears in the gas.

Suppose that a spherical droplet containing A nucleons spontaneously forms in a gas consisting originally of a total number $A+B$ of nucleons. Then,

$$G_{\text{with drop}} = \mu_l A + \mu_g B + 4\pi R^2 \sigma + T\tau \ln A \qquad (3)$$

and

$$G_{\text{no drop}} = \mu_g (A+B) \; . \qquad (4)$$

Here μ_g and μ_l are the chemical potentials for the gas phase and liquid phase, respectively. The third term in Eq. (3) is the surface free energy for a droplet of radius R and with surface tension σ. The last term in Eq. (3) was introduced by Fisher to take into account the fact that the droplet surface closes on itself [10]. This last term is connected to the curvature correction energy which appears in the Myers-Swiatecki formula for the energy of a spherical nucleus (actually the Myers-Swiatecki expression has an $A^{1/3}$ dependence for this term, but we note that for $A \approx 10$ to $A \approx 300$, $A^{1/3} \approx \ln A$ [20]). So the probability of formation of a droplet containing A nucleons is proportional to $\exp(-\Delta G/T)$ where $\Delta G = G_{\text{with drop}} - G_{\text{no drop}}$ and results in a mass yield given by

$$dN/dA = Y_0 \exp\left[\frac{\mu_g - \mu_l}{T} A - \frac{4\pi r_0^2 \sigma}{T} A^{2/3} - \tau \ln A\right] \; , \qquad (5)$$

where Y_0 can be determined imposing total mass conservation. In this model, the surface tension vanishes for temperatures larger than or equal to the critical temperature and one gets for the mass yield

$$dN/dA = Y_0 \exp\left[\frac{\mu_g - \mu_l}{T} A - \tau \ln A\right], \quad T \geq T_c \; . \qquad (6)$$

Furthermore, at the critical temperature, the chemical potentials of the liquid phase and the gas phase are equal and the volume contribution to the Gibbs free energy also vanishes and one obtains at the critical temperature a power law given by

$$dN/dA = Y_0 A^{-\tau}, \quad T = T_c \; . \qquad (7)$$

In Fig. 3 we plot the mass distributions obtained in the

expansion of A=100 nucleus starting with eight different initial temperatures ranging from 2 to 20 MeV and with the ground state density ρ=0.125 fm^{-3}. At each temperature, at least 2000 events were performed in order to generate the mass distributions. Depending on the initial temperature, the system shows different dynamical evolutions, from evaporation-like process (for small temperatures) to fragmentation and complete vaporization processes (large temperatures). Following Eq. (5) we fitted these mass distributions according to

$$dN/dA = Y_0 A^{-\tau} X^{A^{2/3}} Y^A \ , \tag{8}$$

where Y_0, X, Y, and τ are fitting parameters and the fits are shown in Fig. 3 by solid lines. The methodology used to do these fits is as follows. First of all, looking to the log-log plots of the mass distributions at different initial temperatures (Fig. 3), we see that one obtains a linear behavior over almost all the range of masses plotted at the initial temperature T=5 MeV. By fitting this plot with a linear fit, we obtain a slope of -2.23. After that, fixing the parameter τ in Fisher's formula to the value 2.23, we fitted all the mass yields (including T=5 MeV mass yield) using Fisher's formula and considering Y_0, X, and Y as fitting parameters. One sees that Fisher's droplet formula fits the numerical mass distributions quite well over the wide range of temperatures considered here. The values of the fitting parameters are listed in Table I. In this model X is related to the surface tension and is equal to 1 for temperatures larger than or equal to the critical temperature T_c and both X and Y are equal to 1 at the critical temperature. From Table I, we see that the point X=1, Y=1 is obtained in our calculations at $T \approx$4–5 MeV. Note the large difference in the critical temperature with the value obtained in the infinite system. For the system A=400, Fisher's droplet model gives a critical temperature T_c between 5 and 6 MeV. Furthermore, assuming that the surface tension is given by [3,20]

$$\sigma(T) = \sigma(0)\left(1+\frac{3T}{2T_c}\right)\left(1-\frac{T}{T_c}\right)^{3/2} \ , \tag{9}$$

and assuming in our model the critical temperature T_c=5 MeV, we obtain from our fit to the mass distribution at T = 3 MeV a surface tension $\sigma(0) \approx 1$ MeV/fm^2 which is consistent with the experimental value [3,20].

Of course the mass yield shape alone cannot be considered as a conclusive proof for a critical behavior that recalls a phase transition.

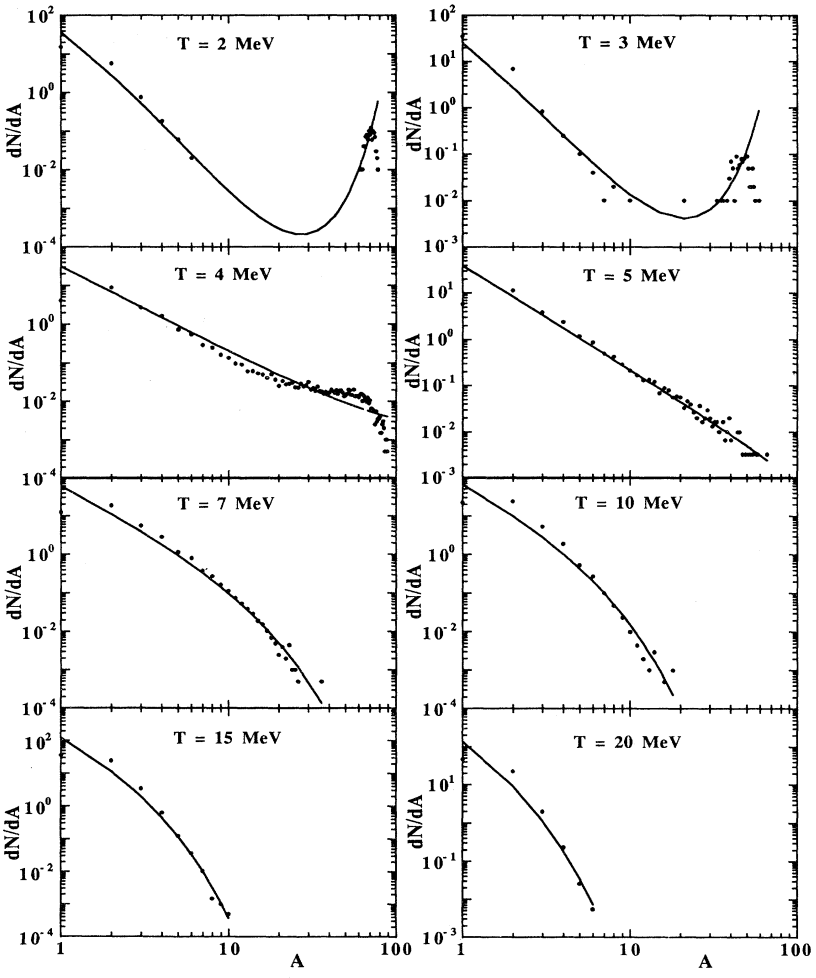

FIG. 3. Mass distributions obtained in the expansion of the system A=100 with eight different initial temperatures ranging from 2 to 20 MeV. The dots in the plot show the results of our calculations and solid lines the fits using Fisher's formula. The calculations are stopped when the anomalous fractal dimensions stabilize (see Sec. VII).

TABLE I. Values of the fitting parameters Y_0, X, Y, and τ entering in the formula Eq. (6).

T (MeV)	2	3	4	5	7	10	15	20
Y_0	442.8	146.1	30.7	39.5	69.7	97.0	290.7	450.5
X	0.042	0.10	1.00	1.00	1.00	1.00	1.00	1.00
Y	2.01	1.83	1.012	0.995	0.87	0.70	0.43	0.31
τ	2.23	2.23	2.23	2.23	2.23	2.23	2.23	2.23

IV. INTERMITTENCY AND ANOMALOUS FRACTAL DIMENSIONS

One of the most powerful and promising methods developed to analyze the fluctuations and the correlations for various physical quantities seems to be the analysis of event-by-event data in terms of intermittency. Intermittency is a statistical concept used to analyze the fluctuations and correlations of a distribution. This concept has been widely recognized in various fields of physics such as turbulent flow [21], astrophysics and magnetohydrodynamics, among others [22,23]. Bialas and Peschanski introduced this idea to study the dynamical fluctuations in rapidity distributions of particles from high-multiplicity events produced in ultrarelativistic reactions [24]. More recently Ploszajczak and Tucholski suggested looking for intermittency in the fragment distributions in nuclear multifragmentation at intermediate energies. They were able to see evidence for an intermittent pattern of fluctuations in the fragment charge distributions both in data and in models [25]. Furthermore, many efforts have been devoted to finding evidence for the occurrence of a phase transition of nuclear matter in the intermittent behavior of the multiplicity distributions [26–28].

Generally, the occurrence of intermittency corresponds to the existence of large nonstatistical fluctuations which have self-similarity over a broad range of scales. This signal can be deduced from the scaled factorial moments which measure the properties of dynamical fluctuations without the bias of statistical fluctuations [24]:

$$F_i(\delta s) = \frac{\sum_{k=1}^{X_{\max}/\delta s} \langle n_k(n_k-1)\cdots(n_k-i+1)\rangle}{\sum_{k=1}^{X_{\max}/\delta s} \langle n_k\rangle^i} \ . \quad (10)$$

Here $X_{\max}$ is an upper characteristic value of the system (i.e., total mass or charge, maximum transverse energy or momentum, etc.) and i is the order of the moment. The total interval $0-X_{\max}$ ($1-A_{\max}$, $Z_{\max}$ in the case of mass or charge distributions) is divided in $M = X_{\max}/\delta s$ bins of size δs, n_k is the number of particles in the kth bin for an event, and the brackets $\langle\ \rangle$ denote the average over many events. If self-similar fluctuations exist at all scales δs, the scaled factorial moments follow the power law $F_i(\delta s) \propto (\delta s)^{-\lambda_i}$ where λ_i are called intermittency exponents. So the intermittent behavior is defined as a linear rise in a plot of $\ln(F_i)$ versus $-\ln(\delta s)$.

Several models have been proposed to describe the multifragmentation of nuclear systems and to study the intermittency signal [25,27,29]. One of the simplest models, widely used in the analysis of experimental data and which gives intermittency, is the percolation model. Percolation models predict a phase transition corrected for finite size effects and produce, at the critical point for this phase transition, a mass distribution following a power law and obeying the scaling properties. It is very interesting to note that the experimental fragment distributions for nuclear multifragmentation reactions exhibit features very similar to those seen in models as simple as percolation.

In Fig. 4 we plot the scaled factorial moments $\ln(F_i)$ versus $-\ln(\delta s)$ for the two studied systems A=100 and A=400. For both systems, at T=7 MeV, the system goes into complete vaporization and the mass distribution has a rather steep slope (see Fig. 3). The logarithm of the scaled factorial moments $\ln(F_i)$ is always negative (i.e., variances are smaller than Poissonian [25,29]) and almost independent of δs and we have no intermittency signal.

For the system A=100, the situation is different for the case T=5 MeV. The logarithms of the scaled factorial moments are positive and almost linearly increasing versus $-\ln(\delta s)$ and the intermittency signal is observed. This case gives intermittency exponents which are of the same order as those reported for the analysis of experimental data and for percolation [25,30]. It is also possible to relate the initial temperature of the expanding system in this model to the q parameter for the bond percolation model. At T=4 and 7 MeV, the behavior of the scaled factorial moments is the same as, in percolation, for subcritical ($q > q_c$) and overcritical ($q < q_c$) events, respectively. The intermittent pattern found at T=5 MeV corresponds to the $q \simeq q_c$ case [25,30].

We observe the same behavior for the system A=400 but the temperature for which we observe a clear intermittency signal is shifted to a higher temperature (T=5.5 MeV). This decreasing of the critical temperature when decreasing the mass of the system (finite size effects) agrees with the results of Jaqaman *et al.* [8].

The presence of large fluctuations as indicated by the intermittency analysis plus the power law in the mass distribution for initial temperatures between 4 and 5 MeV for A=100 and 5 and 6 MeV for A=400 indicate a self-similar behavior both for fluctuations and for averages [31]. These features might be connected to a second-order phase transition in an infinite system. But our system contains a few hundreds of constituents only. To better clarify this point we consider the anomalous fractal dimensions d_i connected to the intermittency exponents λ_i by [23–25]

$$d_i = \lambda_i/(i-1) \ . \quad (11)$$

Different processes seem to give a different behavior of

these anomalous fractal dimensions d_i.

(i) d_i=const corresponds to a monofractal, second-order phase transition in the Ising model and in the Feynman-Wilson fluid [32,33]. In Ref. [34], the authors obtained a similar behavior for the anomalous dimensions using Fisher's free energy for the formation of a droplet in gas [see Eq. (5)].

It has also been demonstrated that in the case of a second-order phase transition in the Ginzburg-Landau (GL) description one gets [33]

$$d_i = d_2\,(i-1)^{\nu-1} \tag{12}$$

with ν=1.304. We note that the GL theory can also be applied to the mean field calculated for our system [15]. In such a case, it can be easily proven that the results obtained in Ref. [33] remain valid in our case when there is no external field; see also the discussion in [3].

(ii) $d_i \propto i$ corresponds to multifractal, cascading processes [24].

Therefore, a study of the anomalous fractal dimensions can give useful information about the evolution of the system [27].

We plot in the upper part of Fig. 5 the anomalous fractal dimensions d, versus i for the system A=100 obtained at different temperatures. At T=4 MeV, the d_i's are negative while they are positive and almost on an increasing straight line for T equal to or larger than 4.5 MeV. Note that the anomalous dimensions d_i have the largest values for the critical temperature T=5 MeV which agrees with the results of Ref. [34]. We have fitted these curves according to Eq. (12) and found ν=2.0, 1.89, and 1.84 at T=4.5, 4.75, and 5 MeV, respectively. A similar estimate, but for the system A=400, gives ν=1.68, 1.75, and 1.74 at T=4, 5, and 6 MeV, respectively. Recall that the value ν=1.304 was obtained in mean field theory and therefore it represents a rough estimate of its actual value. Our calculated values are larger than the GL estimate. Furthermore, increasing the mass of the systems results in ν values closer to the mean field estimate.

In the lower part of Fig. 5 we plot the experimental data obtained in Au fragmentation [25]. Our calculations have the same behavior of the data but are shifted down of a factor of 2. In order to understand the difference between our results and the data we have mixed the events with initial temperatures in the range of 4 to 7 MeV and

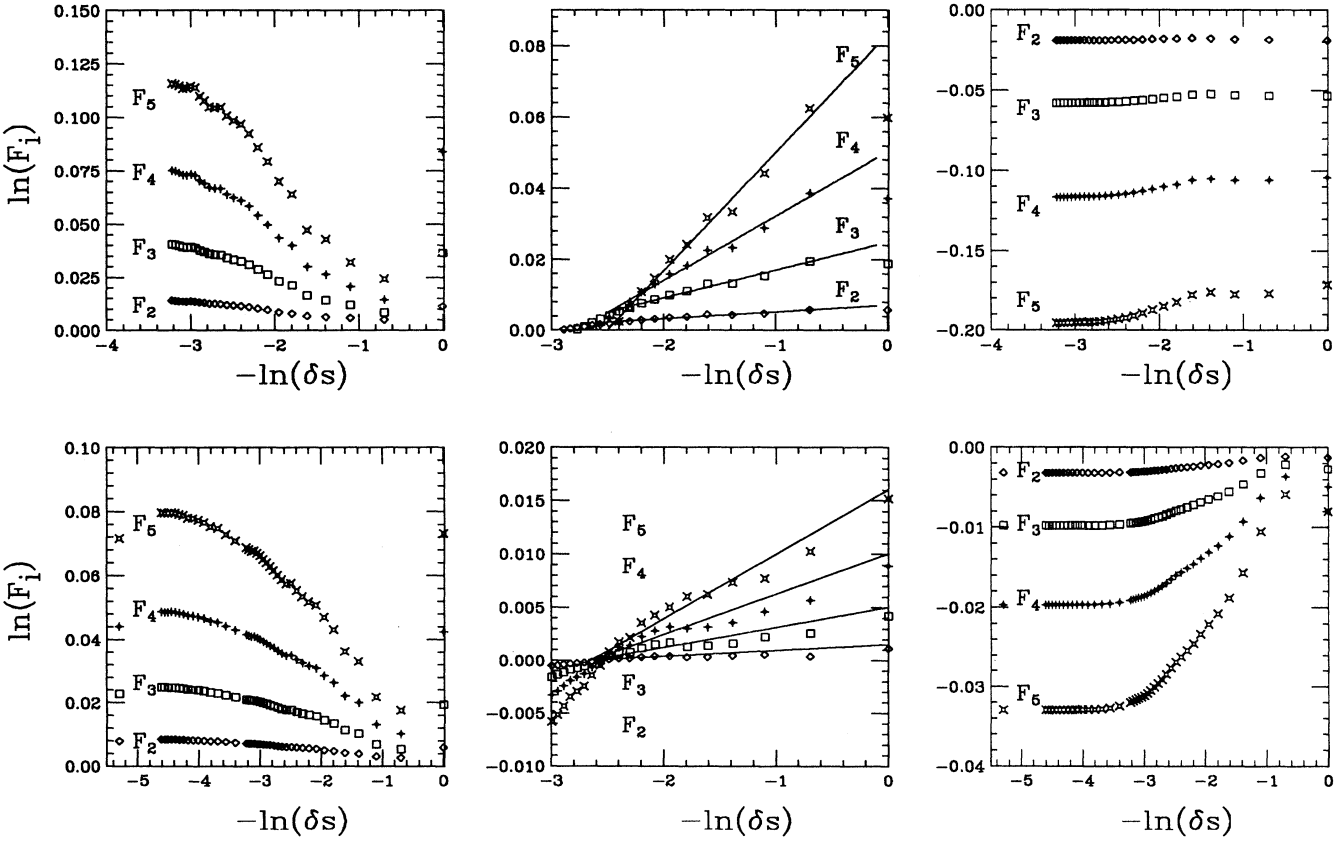

FIG. 4. Logarithm of scaled factorial moments $\ln(F_i)$ versus the logarithm of the bin size $-\ln(\delta s)$ for the expansion of the system A=100 (upper part) starting with temperatures T=4 MeV (left), T=5 MeV (middle), and T=7 MeV (right), and A=400 (lower part) starting with temperatures T=4 MeV (left), T=5.5 MeV (middle), and T=7 MeV (right). The lines in the plot for the system A=100 at T=5 MeV and for the system A=400 at T=5.5 MeV are drawn to guide the eye.

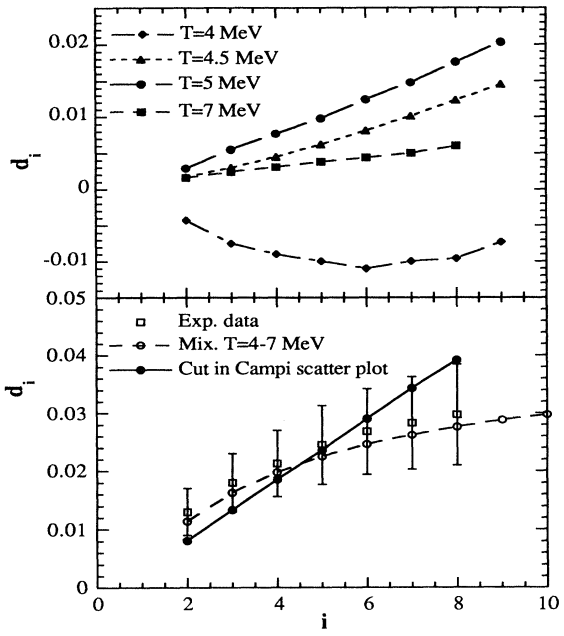

FIG. 5. Anomalous fractal dimensions d_i versus i. In the upper part of the figure, the anomalous dimensions are plotted for different initial temperatures T. In the lower part, open squares represent the experimental data from Ref. [25], open circles our results mixing the events having more than three intermediate mass fragments ($A > 4$) from T=4, 5, 6, and 7 MeV calculations, and solid circles the anomalous dimensions extracted from Fig. 7.

we have chosen only those events having more than three intermediate mass fragments ($A > 4$) similarly to the experimental cuts [25]. The results are shown in the same figure by the open circles. They are in nice agreement with the data and exhibit the feature of being constant for large i values. In previous works [25,27] the apparent flattening of the data, which is in contrast with a cascade process, was related to the possibility of finite size effects. Our results instead indicate that the flattening is solely due to *the mixing of events and to the cuts in the multiplicities.*

V. MOMENTS ANALYSIS

At this point it is worthwhile to use the method of conditional moments developed by Campi [11,12] to better identify the critical behavior observed using Fisher's droplet model and intermittency analysis. As stated in the Introduction, sharp phase transitions are well defined only for an infinite system in that the singularities that are associated with such a transition can only be observed in the thermodynamic limit. If the system has a finite size, the singularities become finite and the transition can be completely washed out by the finite size effects. To overcome this inherent problem of nuclear systems, Campi suggested the method of conditional moments which aims at characterizing the finite system near the critical region in terms of critical exponents, and relations between them are derived for the infinite percolation model. The moments of the cluster size distribution are defined as [11]

$$M_k = \sum_A A^k N(A,\epsilon) \ , \tag{13}$$

where ϵ is a variable characterizing the distance from the critical point. In thermal phase transitions $\epsilon = T_c - T$ is the deviation from the critical temperature T_c while in percolation phase transition $\epsilon = p - p_c$ is the deviation from the threshold probability p_c. $N(A,\epsilon)$ is the multiplicity of the cluster of size A at fixed ϵ.

Near the critical point, a cluster size distribution of the general form

$$N(A,\epsilon) = A^{-\tau} f(\epsilon A^{\sigma}) \tag{14}$$

is predicted where τ and σ are two critical exponents. Fisher's droplet formula, Eq. (5), is a special case of this general form. Replacing the summation in Eq. (13) by an integration, one gets for the moments near the critical point

$$M_k = |\epsilon|^{(\tau-1-k)/\sigma} \ . \tag{15}$$

Since the exponent τ satisfies $2 < \tau < 3$, the second and higher moments diverge at the critical point. In contrast the lower moments M_0 and M_1, which correspond to the number of fragments and the total mass, do not diverge. Furthermore, one cannot define the averaged multiplicity $N(A,\epsilon)$ for a fixed ϵ because there is no model-independent way of classifying the experimental events with respect to ϵ. Therefore, to overcome this difficulty, Campi has proposed to study the moments of single event cluster size distributions

$$M_k^{(j)} = \sum_A A^k n^{(j)}(A) \tag{16}$$

or

$$S_k^{(j)} = M_k^{(j)} / M_1^{(j)} \ , \tag{17}$$

where $n^{(j)}(A)$ is the multiplicity of clusters of size A in the event j, and the summation is over all the fragments in the event *except the heaviest one.* Of course, in finite systems, the moments M_k (or S_k) remain finite, even for $k > 1$. However, if the system keeps some trace of the phase transition for some particular events, the moments M_k should show some strong correlation between them. In particular by studying the correlation in the percolation model and in experimental data between the largest fragment in each event and the second moment of the distribution of the remaining fragments, it was found that this correlation shows the typical features that reflect the occurrence of a phase transition in that it consists of two branches, an upper branch with a negative slope that corresponds in the average to undercritical events ($T < T_c$ in the liquid-gas phase transition, $p > p_c$ in the percolation phase transition) and a lower branch with a positive slope

that corresponds to overcritical events ($T > T_c, p < p_c$). The two branches meet at the critical point of the phase transition [11,27].

In the following, the calculations are done only for the system $A = 100$.

In Fig. 6 we plot the logarithm of the largest cluster P in each event versus the logarithm of the second moment S_2 of the cluster size distribution of the remaining fragments in the event. This plot is generally called Campi scatter plot. The total number of events contributing to this plot is 6000. The events are obtained from CMD simulations with initial temperatures T=4 MeV (2000 events, black points in the figure), T=5 MeV (2000 events, red points), and T=7 MeV (2000 events, blue points). From this figure, one sees clearly the two branches corresponding to undercritical and overcritical events, characteristic of the phase transition observed in percolation and in experimental data. One sees also that the upper branch is made mainly by the events having 4 MeV of initial temperature (black points) while the lower branch is made by the events having 5 and 7 MeV of initial temperature (red and blue points). The region where the two branches meet (which corresponds to the critical region) is made by events coming from calculations with T=4 and 5 MeV of initial temperature (black and red points).

In Fig. 7, we plot the logarithm of the scaled factorial moments calculated from the events which fall within the critical region in the Campi scatter plot Fig. 6 versus the logarithm of the bin size δs. This region is delimited by the yellow rectangle in Fig. 6. One sees from Fig. 6 that the selected events are coming from the CMD simulations with T=4 and 5 MeV. The scaled factorial moments in Fig. 7 show a very strong intermittency signal. The values of the SFM are about six times larger than those obtained with T=5 MeV simulation. In fact, this is obvious because when doing the calculation with T=5 MeV, we are considering a mixture of critical events together with under- and overcritical events due to the statistical fluctuations present in the simulations (see red points in Fig. 6). In this case, the intermittency signal is present because of the presence of critical events but it is weakened due to the presence of noncritical events. In contrast, when making the selection in the Campi scatter plot (Fig. 6), one is mainly selecting the critical events and the intermittency signal is very strong and it is not polluted by the presence of noncritical events. Note that the anomalous fractal dimensions d_i extracted from this figure are within the error bars of the experimental data; see lower part of Fig. 5.

Another test proposed by Campi to have more insight in the shape of the fragment size distributions and to indicate the critical behavior is to look at the relative variance γ_2 defined as [12,25]

$$\gamma_2 = \frac{M_2 M_0}{M_1^2} \,. \tag{18}$$

It was shown by Campi that this quantity presents a peak around the critical point which means that the fluctuations in the fragment size distributions are largest near the critical point [12].

In Fig. 8, we plot the relative variance γ_2 calculated in two different ways versus the reduced multiplicity $n = (M_0 + 1)/A_{\max}$ where $A_{\max}$=100 in this case. In both upper and lower parts of the figure, the open circles show the results for events coming from CMD simulations with initial temperature T=4 MeV, solid circles calculations with T=5 MeV, and open triangles calculations with T=7 MeV. In the upper part of the figure, for a fixed reduced multiplicity n, we calculate the average fragment size distribution $\bar{N}(A, n)$ from all the events having that reduced multiplicity n and calculate the moments M_0,

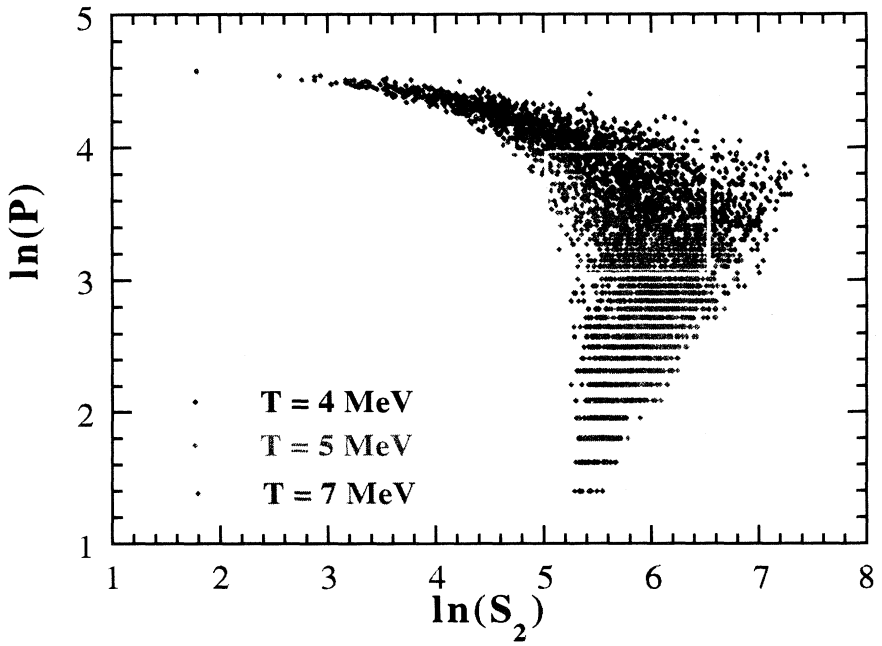

FIG. 6. Campi scatter plot. The logarithm of the largest fragment P in each event is plotted versus the logarithm of the second moment S_2. Black points show events with initial temperature T=4 MeV, red points T=5 MeV, and blue points T=7 MeV. The yellow rectangle delimits the critical region for Fig. 7.

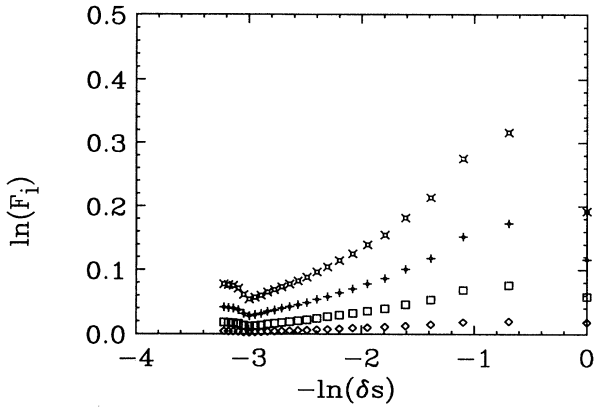

FIG. 7. Scaled factorial moments calculated from the events which fall within the critical region in the Campi scatter plot Fig. 6 (delimited by the yellow rectangle).

M_1, and M_2 as [12]

$$\bar{M}_k = \sum_A A^k \bar{N}(A,n) \tag{19}$$

and $\bar{\gamma}_2$ (inclusive) is given by

$$\bar{\gamma}_2 = \frac{\bar{M}_2 M_0}{\bar{M}_1^2} \ . \tag{20}$$

In the lower part of Fig. 8, we calculate the relative variance $\gamma_2^{(i)}$ for each event i and $\langle\gamma_2\rangle$ (event-by-event) is defined as the average over all the events having the same reduced multiplicity n:

$$\langle\gamma_2\rangle(n) = \frac{1}{N_{\rm ev}(n)} \sum_j \gamma_2^{(j)} \ , \tag{21}$$

where j runs over all events $N_{\rm ev}(n)$ having the reduced multiplicity n. As we have few events with very small multiplicities, one observes some statistical fluctuations for small n. One clearly sees from both upper and lower parts of Fig. 8 that the relative variance γ_2 presents a peak around the reduced multiplicity n=0.15–0.2. One also notes that in both cases, the peak is mainly given by the events having initial temperatures T=4 and 5 MeV (open and solid circles). The results for events with T=7 MeV of initial temperature are located in the tail of the distribution, far from the peak. We notice also that around the peak, $\bar{\gamma}_2$ has larger values than $\langle\gamma_2\rangle$. This effect has also been seen in percolation [35].

Finally we plot in Fig. 9 the two relative variances $\bar{\gamma}_2$ (dashed line) and $\langle\gamma_2\rangle$ (solid line) defined above versus the initial temperature in our calculations. The reduced multiplicity used above is replaced here by the initial temperature for the expansion of our system. So now the two γ_2 are defined as

$$\bar{\gamma}_2 = \frac{\bar{M}_2 \bar{M}_0}{\bar{M}_1^2} \ , \tag{22}$$

where the moments $\bar{M}_0$, $\bar{M}_1$, and $\bar{M}_2$ are given by

$$\bar{M}_k = \sum_A A^k \bar{N}(A,T) \tag{23}$$

and

$$\langle\gamma_2\rangle(T) = \frac{1}{N_{\rm ev}(T)} \sum_j \gamma_2^{(j)} \ , \tag{24}$$

where j runs over all events $N_{\rm ev}(T)$ having the initial temperature T. One sees that both curves show a peak for temperatures between 4 and 5 MeV. Note again that $\bar{\gamma}_2$ gives larger values than $\langle\gamma_2\rangle$.

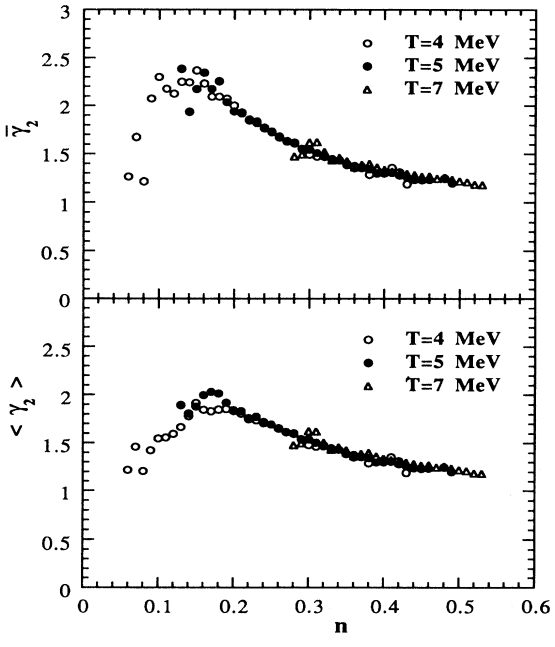

FIG. 8. Reduced variance γ_2 versus reduced multiplicity n for the system A=100. In both parts of the figure, open circles show the results for events with initial temperature T=4 MeV, solid circles T=5 MeV, and open triangles T=7 MeV. See text for the definition of $\bar{\gamma}_2$ and $\langle\gamma_2\rangle$.

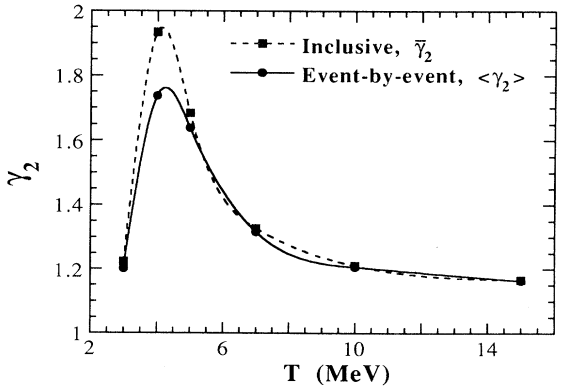

FIG. 9. Reduced variance γ_2 versus the initial temperature T of the expansion of the system A=100. Dashed line shows the results for $\bar{\gamma}_2$ and solid line $\langle\gamma_2\rangle$.

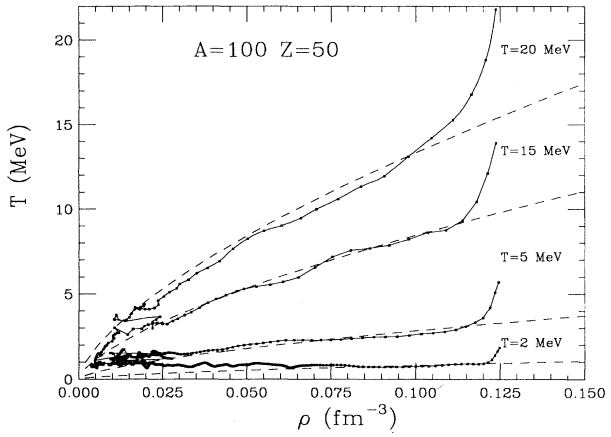

FIG. 10. Expansion with Coulomb interaction included in the dynamics of a system with A=100, Z=50 starting from temperatures T=2, 5, 15, and 20 MeV. The average temperature of the biggest fragment is plotted versus its average density.

VI. ROLE OF THE COULOMB FORCE

As we can intuitively expect there should be important differences when the system under consideration is charged. The reason why in nature infinitely large nuclei do not exist is because of the strong repulsion among protons. In fact, in order to keep the binding energy per nucleon almost constant in natural atoms, the ratio of neutrons to protons changes. Thus we can also expect a critical behavior in a nucleus-nucleus collision when a highly charged fragment is not formed. For example, in Au+Au collisions there should be no multifragmentation of the total system, but the projectile or the target opportunely excited might go into multifragmentation. To shed more light about this problem we repeated the calculation of an expanding A=100 system, with half of the constituents charged. In Fig. 10 we plot the time evolution of the charged system in the (ρ, T) plane. Note the large difference with the uncharged expanding system for the case T=2 MeV, Fig. 1. This case is an evaporation case if there is no Coulomb field. But when charging the system, the extra positive pressure due to Coulomb pushes the system towards lower densities, thus entering the instability region. In Fig. 11 we plot the mass distributions corresponding to different initial temperatures together with the factorial moments. We see a qualitatively similar behavior with the cases without Coulomb field but everything is shifted to lower temperatures. The shift is roughly 3 MeV down, i.e., the critical behavior is observed for T about 2–3 MeV. We would like to stress that for a charged system there is no reason why one should get a power law in the mass distribution for the most critical events. We can see that the factorial moments show an intermittent behavior for temperatures

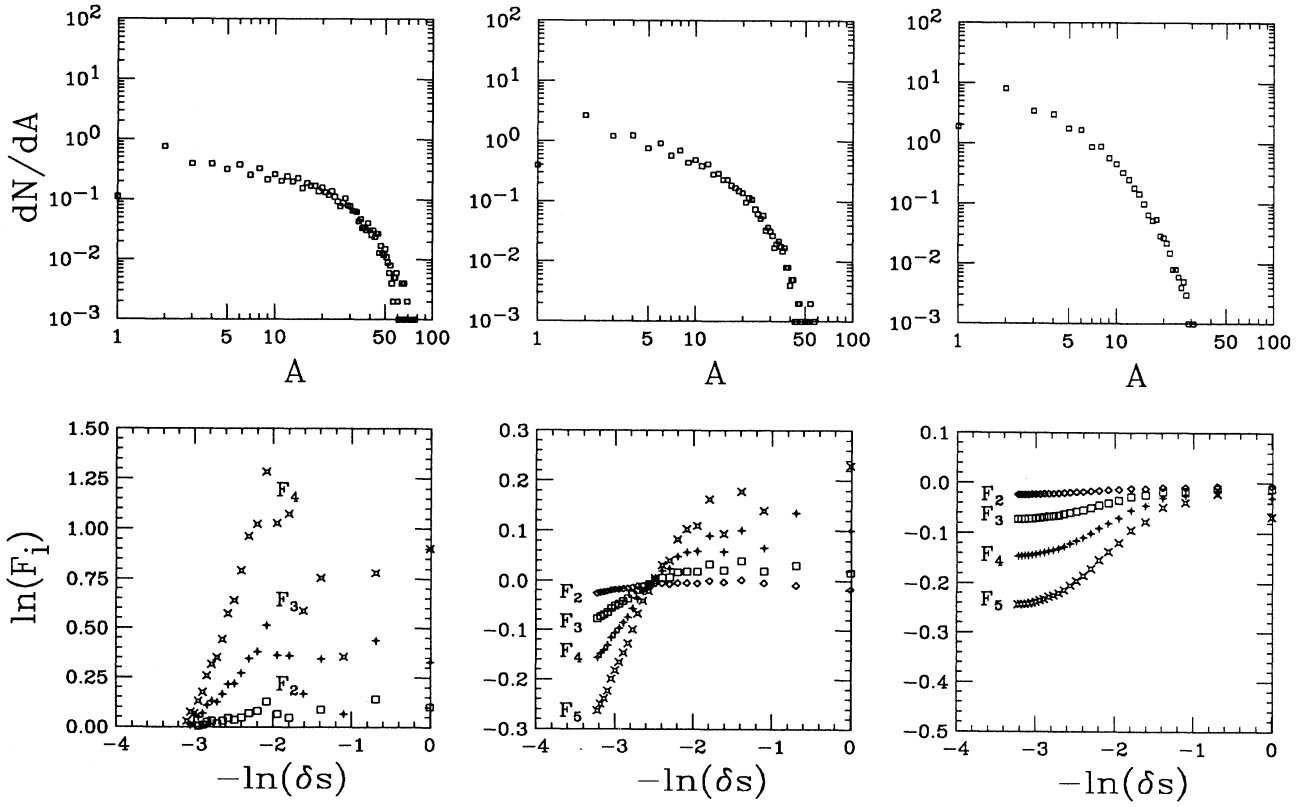

FIG. 11. Expansion with Coulomb of the system A=100, Z=50. Mass distributions and the corresponding scaled factorial moments $\ln(F_i)$ versus $-\ln(\delta s)$ for events with initial temperatures T=1.5 (left), 2 (center), and 3 MeV (right).

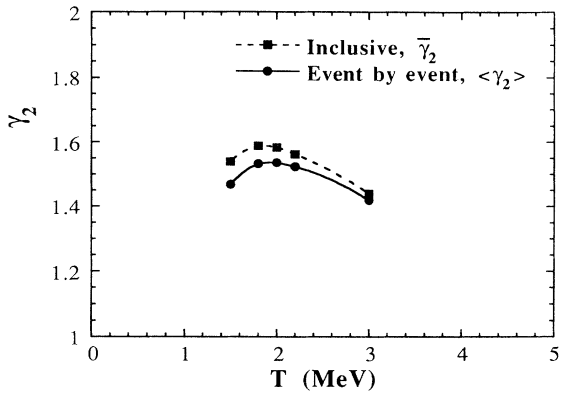

FIG. 12. Expansion with Coulomb. Reduced variance γ_2 versus initial temperature T. Dashed line shows $\bar{\gamma}_2$ and solid line $\langle\gamma_2\rangle$.

around 2 MeV, Fig. 11. The shift to lower temperatures is more clearly demonstrated in Fig. 12 where the reduced variance is plotted versus temperature T. Comparing to the analogous case without Coulomb charge, Fig. 9, we see clearly the shift towards lower temperatures.

We would like to discuss some analogies and differences of our molecular dynamics approach with some successful statistical models widely applied to nuclear multifragmentation [27,36]. As we demonstrated in Fig. 2, the multiplicity increases suddenly in the T=5 MeV case, for example. This implies that the breaking of the system happens almost simultaneously and later on there is some evaporation that cools down the fragments. This is one of the basic assumptions of the statistical models. From our calculations we find that the density of the biggest fragment and its temperature when the multiplicity sharply increases is about 0.025 fm^{-3} and 2 MeV, respectively. These values probably depend on the two-body forces we are using and in particular on the range of the force itself; thus we do not try to compare these values with those used in statistical models. One difference with statistical models is the role of the Coulomb force. In our case the excitation energy the system needs to go into multifragmentation is lower since the extra push given by Coulomb helps the system to climb the barrier. A consequence of this is that the time it takes to reach the multifragmentation point is much larger in the Coulomb case. At lower temperatures the expansion is very slow, so it takes a long time before the system reaches the point where it is unstable, more than a few hundreds fm/c. However, in statistical models one usually determines the configuration of the system at the freeze-out and then calculates the Coulomb trajectories of the fragments. So Coulomb plays a role only for the final angles, kinetic energies, etc., of the fragments while in molecular dynamics it plays a role for the entire dynamics.

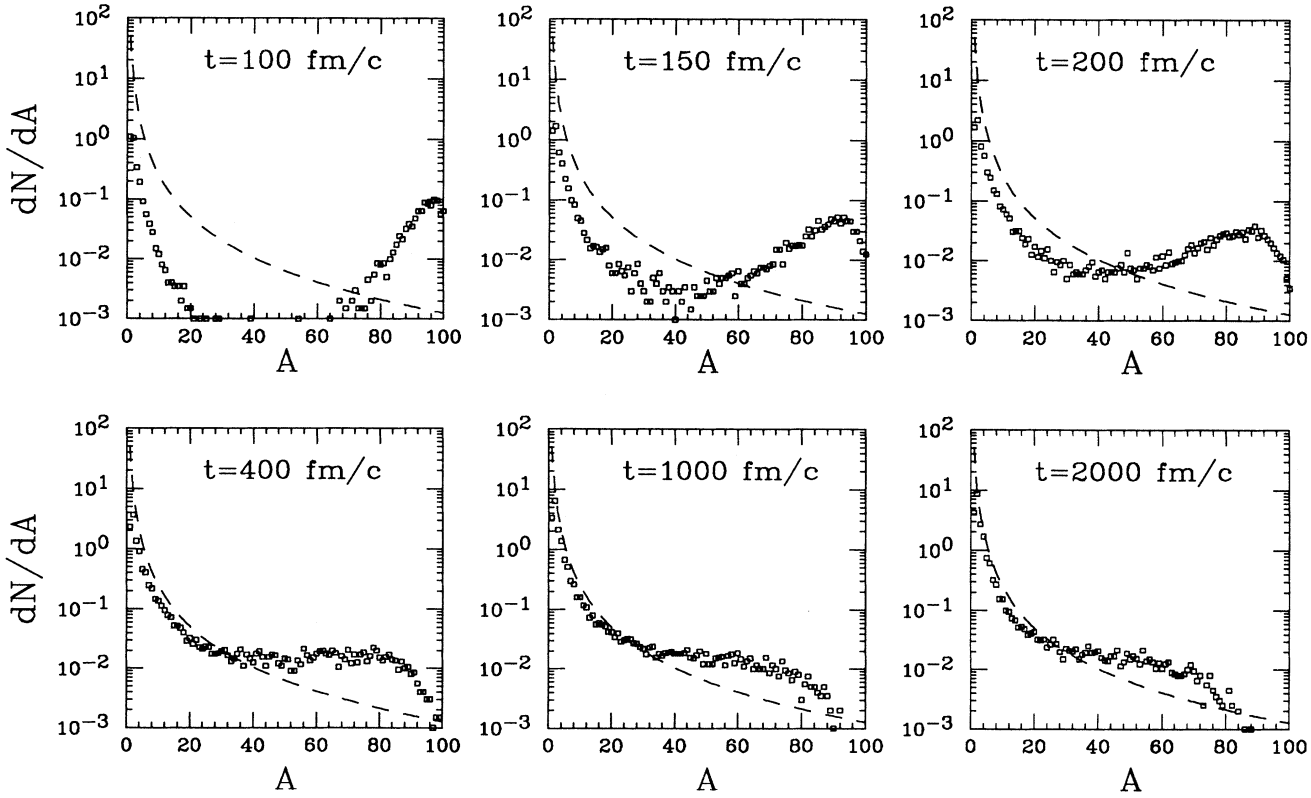

FIG. 13. Mass distributions at different times during the expansion of the system A=100 starting with an initial temperature T=4 MeV. The dashed lines give a power law yield.

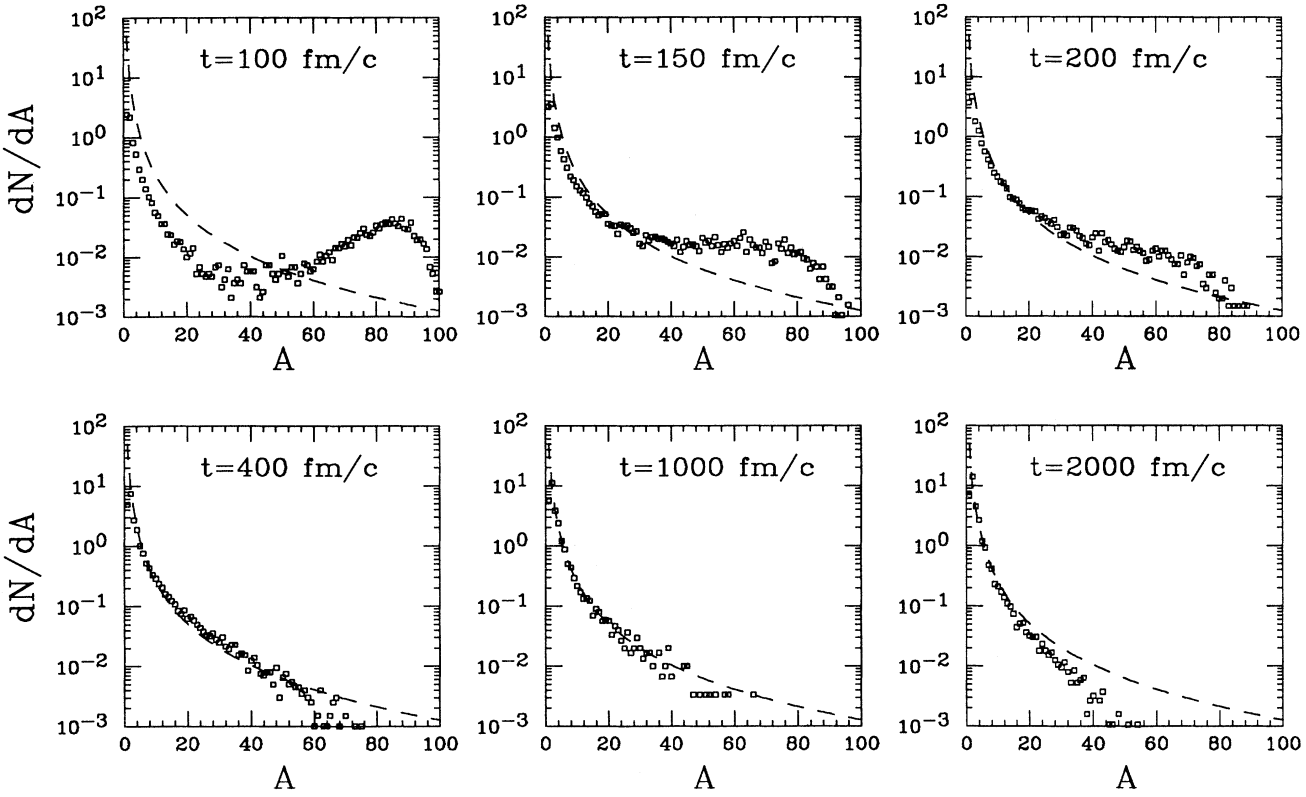

FIG. 14. Same as Fig. 13 but with an initial temperature T=5 MeV.

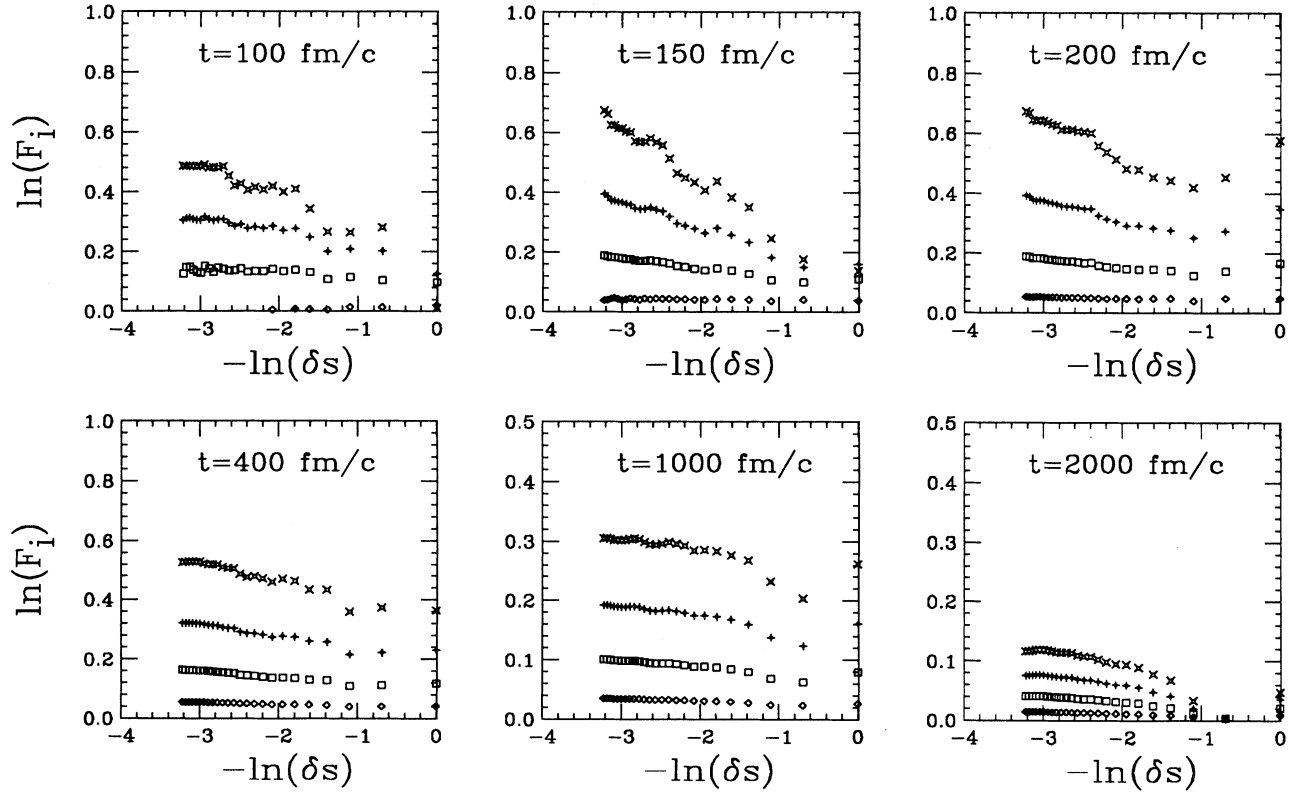

FIG. 15. Scaled factorial moments at different times during the expansion of the system A=100 starting with an initial temperature T=4 MeV.

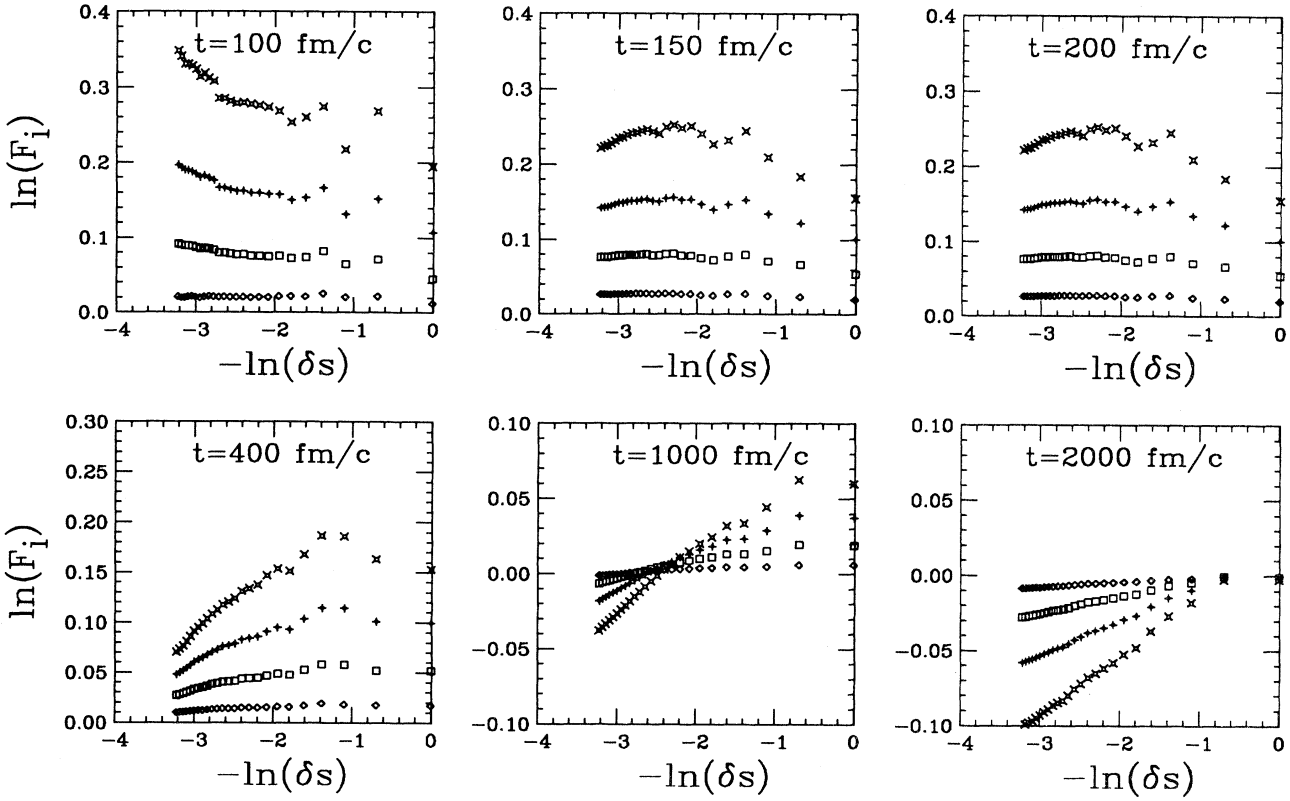

FIG. 16. Same as Fig. 15 but with an initial temperature T=5 MeV.

VII. TIME EVOLUTION OF INSTABILITIES

In this section we would like to discuss in more detail the time evolution of the expanding system. Here we will treat cases without Coulomb force included. In Figs. 13 and 14 we plot the mass yield for the T=4 and 5 MeV cases, respectively, at various times. The dashed line gives a power law yield. In order to have a better picture of the time evolution of the system we plot in Figs. 15 and 16 the factorial moments for the same times and temperatures as for the mass yields. We observe that at about the time when we have a large multiplicity of fragments (see Fig. 2), i.e., t=100 fm/c, the factorial moments are positive but almost flat. Recall that the factorial moments are equal to one for a Poissonian distribution. Thus we have fluctuations larger than Poissonian already at such an early time. Note that in the T=4 MeV case the slope of the factorial moments is inverted as compared to the T=5 MeV case and the absolute values of $\ln F_i$ are larger. If we look now at the corresponding mass distribution we observe at t=100 fm/c the presence of bigger fragments in the T=4 MeV case, i.e., more liquid than vapor as compared to the T=5 MeV case. The presence of large drops of liquid at T=4 MeV, in the final fragments distribution, is probably responsible for the opposite slopes in the two cases. An interesting feature is that when the mass yield follows exactly a power law (T=5 MeV, t=400 fm/c) we also have a power law in the factorial

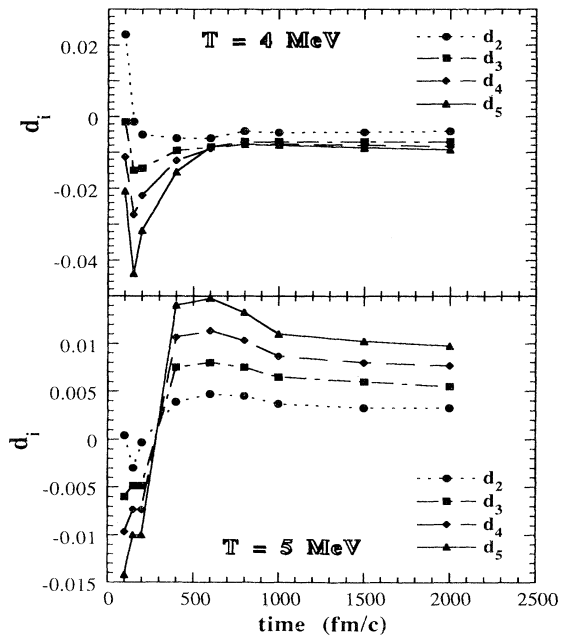

FIG. 17. Time evolution of anomalous fractal dimensions d_i. The upper part of the figure shows the results for the expansion of the system A=100 starting with an initial temperature T=4 MeV and the lower part with an initial temperature T=5 MeV.

moments. Another important aspect to keep in mind, especially when analyzing experimental data where only the final fragment distribution is given, is the decrease of the values of the factorial moments with increasing time. Note, however, that the slopes remain almost constant after some time. The reason why the values of the factorial moments are decreasing is essentially evaporation. Since we have a small system, excited fragments emit nucleons, deuterons, etc., and therefore "fill up" small masses bins and "empty out" large masses bins. The factorial moments are especially sensitive to smaller masses (because they have larger yields); therefore, their values decrease because of these secondary decays. However, the secondary decays have almost the same effects for the small bins and the slope of the factorial moments does not change. This can be clearly seen in Fig. 17 where we plot the anomalous fractal dimensions d_i versus time for the two temperatures. Note, as we have stated, that the d_i's are negative in the T=4 MeV case but positive in the T=5 MeV case. Furthermore, these indices saturate rather quickly and therefore are insensitive to secondary decays. It seems to us that these indices are the most representative of a critical behavior of a finite system since, as observed, they are insensitive to fragments evaporation in contrast to mass distributions and factorial moments.

VIII. CONCLUSIONS

In conclusion, we have found evidence for a critical behavior in finite systems in a dynamical model. Under some initial conditions, the dynamical evolution creates a power law mass distribution of fragments with τ=2.23 and develops an intermittent pattern of fluctuations. We have used a moment analysis of the distribution to further substantiate the large fluctuations for our finite system, and we have also performed a dynamical analysis to shed some light on the critical behavior. A very great similarity with the results obtained for the percolation model is found for many aspects. We have stressed the important role played by the Coulomb field in shifting the point of critical multifragmentation towards lower excitation energies. The time evolution of a system undergoing multifragmentation, as described by this molecular dynamics approach, demonstrates rather clearly that the most important observables are the fractal anomalous dimensions and the Campi plots since they are rather insensitive to the latest stage of the evolution, i.e., the final cooling of the fragments through evaporation. We hope that the results discussed in this article might be useful to the experimentalist in analyzing data on nucleus-nucleus collisions in an almost 4π geometry.

[1] M. W. Curtain, H. Toki, and D. K. Scott, Phys. Lett. **123B**, 289 (1983); A. D. Panagiotou, M. W. Curtain, H. Toki, D. K. Scott, and P. J. Siemens, Phys. Rev. Lett. **52**, 496 (1984).

[2] G. F. Bertsch and P. J. Siemens, Phys. Lett. **126B**, 9 (1983).

[3] A. L. Goodman, J. I. Kapusta, and A. Z. Mekjian, Phys. Rev. C **30**, 851 (1984).

[4] H. R. Jaqaman, Gabor Papp, and D. H. E. Gross, Nucl. Phys. **A514**, 327 (1990).

[5] R. G. Palmer and P. W. Anderson, Phys. Rev. D **9**, 3281 (1974); W. G. Kupper, G. Wegmann, and E. R. Hilf, Ann. Phys. (N.Y.) **88**, 454 (1974); G. Sauer, H. Chandra, and U. Mosel, Nucl. Phys. **A264**, 221 (1976).

[6] P. Danielewicz, Nucl. Phys. **A314**, 465 (1979).

[7] D. Q. Lamb, J. M. Lattimer, C. J. Pethick, and D. G. Ravenhall, Phys. Lett. **41**, 1623 (1978); Nucl. Phys. **A360**, 459 (1981); H. Schulz, L. Münchow, G. Röpke, and M. Schmidt, Phys. Lett. **119B**, 12 (1982); Nucl. Phys. **A399**, 587 (1983).

[8] H. R. Jaqaman, A. Z. Mekjian, and L. Zamick, Phys. Rev. C **27**, 2782 (1983); **29**, 2067 (1984).

[9] J. E. Finn *et al.*, Phys. Rev. Lett. **49**, 1321 (1982); Phys. Lett. **118B**, 458 (1982); H. H. Gutbrod, A. I. Warwick, and H. Wieman, Nucl. Phys. **A387**, 177c (1982); M. Mahi, A. T. Bujak, D. D. Carmony, Y. H. Chung, L. J. Gutay, A. S. Hirsch, G. L. Paderewski, N. T. Porile, T. C. Sangster, R. P. Scharenberg, and B. C. Stringfellow, Phys. Rev. Lett. **60**, 1936 (1988); J. B. Elliot, M. L. Gilkes, J. A. Hauger, A. S. Hirsch, E. Hjort, N. T. Porile, R. P. Scharenberg, B. K. Srivastava, M. L. Tincknell, and P. G. Warren, Phys. Rev. C **49**, 3185 (1984); M. L. Gilkes *et al.*, Phys. Rev. Lett. **73**, 1590 (1994).

[10] M. E. Fisher, Rep. Prog. Phys. **30**, 615 (1967); *Critical Phenomena*, Proceedings of the International School of Physics "Enrico Fermi," Course LI, edited by M. S. Green (Academic, New York, 1971).

[11] X. Campi, J. Phys. A **19**, L917 (1986).

[12] X. Campi, Phys. Lett. B **208**, 351 (1988); J. Phys. (Paris) **50**, 183 (1989).

[13] A. Bonasera, F. Gulminelli, and J. Molitoris, Phys. Rep. **243**, 1 (1994).

[14] M. Belkacem, V. Latora, and A. Bonasera, Phys. Lett. B **326**, 21 (1994).

[15] R. J. Lenk, T. J. Schlagel, and V. R. Pandharipande, Phys. Rev. C **42**, 372 (1990).

[16] V. Latora, A. Del Zoppo, and A. Bonasera, Nucl. Phys. **A572**, 477 (1994).

[17] S. E. Koonin and D. C. Meredith, *Computational Physics* (Addison Wesley, Redwood City, California, 1990).

[18] L. Wilet, E. M. Henley, M. Kraft, and A. D. MacKellar, Nucl. Phys. **A282**, 341 (1977); H. Horiuchi, *ibid.* **A522**, 257c (1991).

[19] A. Vicentini, G. Jacucci, and V. R. Pandharipande, Phys. Rev. C **31**, 1783 (1985).

[20] A. R. DeAngelis and A. Z. Mekjian, in *Relativistic Heavy-Ion Physics*, edited by L. P. Csernai and D. D. Strottman, International Review of Nuclear Physics Vol. 6 (World Scientific, Singapore, 1991), p. 363.

[21] B. Mandelbrot, J. Fluid Mech. **62**, 331 (1974).

[22] Ya. B. Zeldovich, S. A. Molchanov, A. A. Ruzmaikin, and D. D. Sokoloff, Usp. Fiz. Nauk. **152**, 3 (1987) [Sov. Phys. Usp. **30**, 353 (1987)].

[23] D. H. E. Gross, Nucl. Phys. **A553**, 175c (1993); L. P. Kadanoff, Physica A **163**, 1 (1990); A. Bialas, Nucl. Phys. **A525**, 345 (1991), and references therein.

[24] A. Bialas and R. Peschanski, Nucl. Phys. **B273**, 703 (1986); **B308**, 857 (1988).

[25] M. Ploszajczak and A. Tucholski, Phys. Rev. Lett. **65**, 1539 (1990); Nucl. Phys. **A523**, 651 (1991).
[26] A. Bialas and R. C. Hwa, Phys. Lett. B **253**, 436 (1991).
[27] H. R. Jaqaman and D. H. E. Gross, Nucl. Phys. **A524**, 321 (1991); D. H. E. Gross, A. R. DeAngelis, H. R. Jaqaman, Pan Jicai, and R. Heck, Phys. Rev. Lett. **68**, 146 (1992); A. R. DeAngelis, D. H. E. Gross, and R. Heck, Nucl. Phys. **A537**, 606 (1992).
[28] V. Latora, M. Belkacem, and A. Bonasera, Phys. Rev. Lett. **73**, 1765 (1994).
[29] H. W. Barz, J. P. Bondorf, R. Donangelo, I. N. Mishustin, H. Schulz, and K. Sneppen, Phys. Rev. C **45**, 2541 (1992).
[30] M. Baldo, A. Causa, and A. Rapisarda, Phys. Rev. C **48**, 2520 (1993).
[31] B. Elattari, J. Richert, and P. Wagner, Phys. Rev. Lett. **69**, 45 (1992); Nucl. Phys. **A560**, 603 (1993).
[32] H. Satz, Nucl. Phys. **B326**, 613 (1989).
[33] R. C. Hwa and M. T. Nazirov, Phys. Rev. Lett. **69**, 741 (1992).
[34] T. Kubo, M. Belkacem, V. Latora, and A. Bonasera, Z. Phys. A (to be published).
[35] X. Campi and H. Khrivine, private communication.
[36] J. P. Bondorf, R. Donangelo, I. N. Mishustin, C. J. Pethick, H. Schulz, and K. Sneppen, Nucl. Phys. **A443**, 321 (1985); J. P. Bondorf, R. Donangelo, I. N. Mishustin, and H. Schulz, *ibid.* **A444**, 460 (1985).

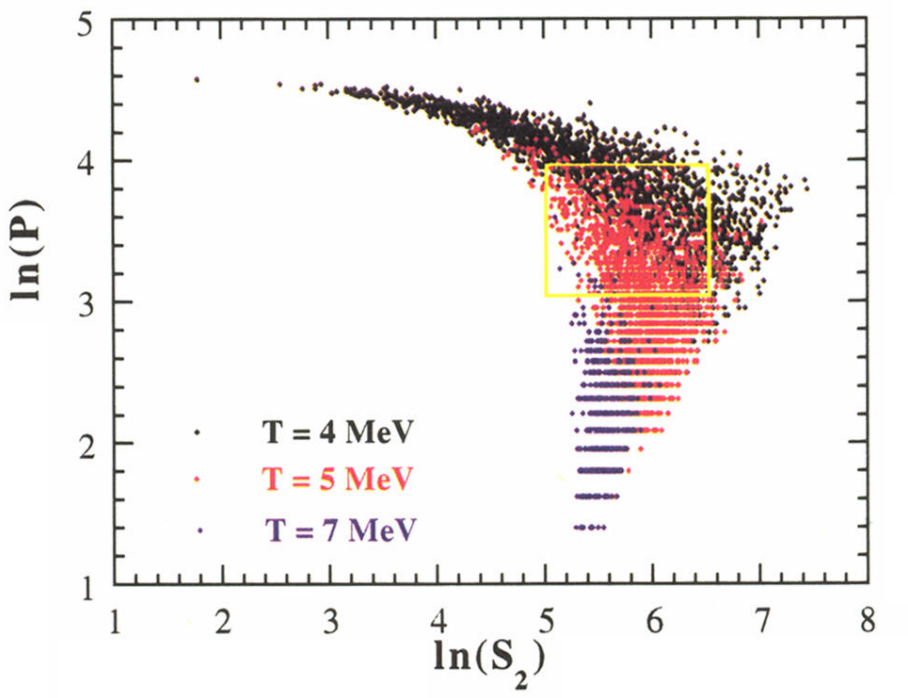

FIG. 6. Campi scatter plot. The logarithm of the largest fragment P in each event is plotted versus the logarithm of the second moment S_2. Black points show events with initial temperature T=4 MeV, red points T=5 MeV, and blue points T=7 MeV. The yellow rectangle delimits the critical region for Fig. 7.